Nanoscale

PAPER

View Article Online
View Journal

Cite this: DOI: 10.1039/d0nr08998b

Anisotropic nanoporous morphology of ZnO-supported Co that enhances catalytic activity†

Christopher M. Coaty, ‡[a] Adam A. Corrao, ‡[b,c] Victoria Petrova, ‡[a] Taewoo Kim, [d] David P. Fenning,[a,d,e,f] Peter G. Khalifah *[b,c] and Ping Liu *[a,d,f]

Received 21st December 2020,
Accepted 17th April 2021

DOI: 10.1039/d0nr08998b

rsc.li/nanoscale

A novel conversion reaction synthesis (CRS) method is used to synthesize ZnO-supported Co nanoporous metal hybrid structures from a co-precipitated nanocomposite precursor of ZnO and Co_3O_4. After removal of Li_2O with water, the resulting material consists of ZnO-supported Co nanoparticles that are interconnected to form anisotropic micro-particles. Additionally, individual ZnO nanoparticles have an anisotropic morphology, as revealed by synchrotron XRD analysis. Microscopy and surface area studies show these materials have an average pore size of 10–30 nm and specific surface areas up to 28 $m^2\ g^{-1}$. The hybrid structure also has increased heat resistance compared to that of pure nanoporous metals; the Co phase within the ZnO–Co hybrid exhibits much less coarsening than the analogous nanoporous metal without ZnO at temperatures of 400 °C and above. These ZnO–Co hybrid materials were tested as heterogeneous catalysts for the steam reformation of ethanol at 400 °C. The nanoporous ZnO–Co hybrid material exhibits complete conversion of ethanol and high hydrogen selectivity, producing H_2 with a molar yield of approximately 70%.

Introduction

For materials being used as catalysts (*e.g.*, heterogeneous catalysis, electrocatalysis), it has been long recognized that catalytic activity increases with increasing surface area.[1–3] For this reason, extensive efforts have been devoted to the preparation of catalyst materials in the form of nanoparticles (NP) which can have exceptionally high surface areas.[4–6] However, these NP catalysts have been found to suffer from a variety of limitations due to their morphology, which has a tendency to coarsen and lose activity during extended use due to a lack of physical stability. This effect can also lead to to toxicity concerns due to the ease with which nanoparticles can be inhaled or ingested due to their exceptionally small particle sizes.[7] For these reasons, extensive efforts have been devoted to developing good support materials for nanoparticles, though the support materials add both cost and complexity to the system as well as limiting the achievable mass loading. More recently, the field of catalysis has begun exploring an alternate nanoporous (NPo) morphology that overcomes many of the limitations of nanoparticles.[8] NPo materials can retain the very high surface areas desired for catalysis while having greatly enhanced stability relative to isolated NPs due to their large micron-scale secondary particles constructed from nanoscale primary particles of interconnected material ligaments.

Despite the strong advantages of nanoporous materials over nanoparticle materials, further advances in their preparation are required to fully unlock their potential for catalytic applications. First, NPo materials have so far only been prepared in the form of isotropic particles. In the case of micron-sized particles, there are expected to be very significant diffusion limitations both in reactants reaching the inner core of the particle and in products diffusing out from the core, resulting in decreased catalytic rates. However, if the NPo material can be prepared with an anisotropic morphology such as a rod or a plate, the time required for species to diffuse between the inner core and the outer surface can be significantly reduced. To date, there has only been limited top-down synthetic work to assemble nanoparticles into anisotropic architectures,[9] and there have been no reports of bottom-up synthesis routes for the preparation of anisotropic NPo materials that can effectively utilize their entire interior surface area.

[a]*Department of Nanoengineering, University of California San Diego, La Jolla, CA 92093, USA. E-mail: piliu@eng.ucsd.edu*
[b]*Department of Chemistry, Stony Brook University, Stony Brook, NY 11794, USA. E-mail: kpete@bnl.gov*
[c]*Chemistry Division, Brookhaven National Lab, Upton, NY 11973, USA*
[d]*Chemical Engineering Program, Department of Nanoengineering, University of California San Diego, La Jolla, CA 92093, USA*
[e]*Materials Science Program, University of California San Diego, La Jolla, California 92093, USA*
[f]*Sustainable Power and Energy Center, University of California San Diego, La Jolla, California 92093, USA*
†Electronic supplementary information (ESI) available. See DOI: 10.1039/d0nr08998b
‡These authors contributed equally to this work.

Second, methods for improving the temperature stability of NPo systems are needed. Although NPo metals such as Au and Cu are widely studied as electrocatalysts,[8] it is much less common to see them employed as heterogeneous catalysts despite the success of examples like RANEY® nickel as an important catalyst for industrial hydrogenation.[10,11] One reason for this is that NPo metals tend to sinter and coarsen at elevated temperatures, sometimes at temperatures as low as 100 °C,[12,13] and prolonged usage decreases surface area which subsequently decreases catalytic activity. Successful implementations of NPo materials as heterogeneous catalysts are typically in lower temperature applications, *i.e.*, the catalytic activity of pure nanoporous gold for glucose oxidation between −30 °C and 30 °C.[10,14] One approach to make NPo metals more compatible with high temperature applications is to combine them with non-metals such as metal oxides to stabilize the metal phase at higher temperatures, as has been done for traditional NP catalysts. Metal oxide supports have previously been used with NPs to add synergistic functionality (*e.g.*, acidic or basic surfaces) that improve catalytic efficiency and selectivity.[15–17]

Third, more versatile synthesis methods are needed. One limitation of the dominant dealloying method used for the preparation of NPo materials is that it can only be used to produce a limited subset of metallic materials that are generally the most noble metals.[18–20] A second limitation of conventional dealloying methods is that the products are produced on a small scale of milligrams or grams, rather than on the scale of kilograms or metric tons that industry may require. We have recently demonstrated a new conversion reaction synthesis (CRS) method that can overcome both of these limitations in the applicability of NPo materials to catalysis, as the steps involved in CRS synthesis are both scalable and have been demonstrated to work for a wide range of metallic materials.[13,21]

The CRS approach has to date been utilized to prepare NPo metals with pores ranging from 1–100 nm in diameter from simple starting materials that can be obtained in bulk quantities. This synthesis method uses a strong reducing agent added to a non-polar solvent in which the precursor particles are suspended and converted into a nanocomposite comprised of two intermixed nanocrystalline phases. One of these phases is then selectively dissolved with a suitable solvent, leaving the insoluble phase behind with a nanoporous morphology. For example, the reduction of $CoCl_2$ particles suspended in hexane with *n*-butyllithium (*n*-BuLi) produces a metal-salt nanocomposite of Co and LiCl, the latter of which can be removed by washing with alcohol to leave micron-size nanoporous Co particles with pore sizes of about 15 nm.[21] The net redox reaction scheme is given below in eqn (1) and (2):

$$\underset{[\text{metal} - \text{salt nanocomposite}]}{CoCl_2(s) + 2Li \rightarrow Co(s) + 2LiCl(s)} \quad (1)$$

$$Co(s) + 2LiCl(s) + \text{rinse} \rightarrow Co(s)\ [\text{nanoporous metal}] \quad (2)$$

Although the CRS methods previously used for preparing nanoporous metals have exclusively involved salt precursors (*e.g.*, $CoCl_2$) and salt products (*e.g.*, LiCl), in theory any type of ionic compound that can be reduced in the solid phase to produce a nanocomposite with at least one easily removable product phase can be used to produce nanoporous systems.

In this work, we demonstrate a modified version of the CRS for producing nanoporous hybrid materials containing both metal and metal oxide components with a highly anisotropic morphology that is demonstrated to be effective for heterogeneous catalysis. Specifically, this work demonstrates the synthesis of ZnO-supported Co metal (ZOC) through the reduction of ZnO–Co_3O_4 composites prepared through co-precipitation. The resulting nanoporous hybrid material addresses all three major limitations in the use of nanoporous metals for heterogeneous catalysis and represents both the first CRS synthesis of metal–metal oxide hybrids and the first CRS synthesis of anisotropic rod-shaped particles. ZOC is employed as an efficient catalyst for the steam reformation of ethanol to produce hydrogen; its advantage over an isotropic analogue is clearly demonstrated.

Results and discussion

In this work, the central goal is to develop new synthetic approaches to address the major limitations involved in the preparation of nanoporous (NPo) materials for use as heterogeneous catalysts, specifically (1) developing anisotropic morphologies, (2) integrating oxide supports to enhance stability, and (3) using a scalable and versatile approach that can access a wide range of chemistries. We chose ZnO-supported Co metal (ZOC) as an initial synthetic target since this is a known catalyst for the steam reformation of ethanol (SRE) whose activity can readily be tested.[22–24] The preparation of ZOC was done using a modified CRS in which a co-precipitated ZnO–Co_3O_4 precursor was reduced with *n*-BuLi through the overall (unbalanced) expected reaction scheme given below in eqn (3). Dissolving the reaction intermediates with water should leave Zn-supported Co metal as the sole product (eqn (4)).

$$\underset{[\text{nanocomposite hybrid}]}{Co_3O_4 : ZnO + Li \rightarrow Co : ZnO + Li_2O} \quad (3)$$

$$\underset{[\text{nanoporous hybrid}]}{Co : ZnO + Li_2O + \text{rinse} \rightarrow Co : ZnO} \quad (4)$$

In contrast to prior CRS methods for producing nanoporous metals, the present reaction scheme involves more than one metal species. The reaction is designed so that the less electropositive cobalt oxide precursor will be reduced to cobalt metal while the more electropositive Zn oxide precursor will not be reduced and instead will remain as an oxide support for Co metal. It is hypothesized that ZnO will stabilize the nanostructured Co phase and allow it to resist coarsening when exposed to high temperatures. Furthermore, ZnO crystallites often have anisotropic shapes due to their symmetry[25–27] which may provide a route to realizing anisotropic secondary particle morphologies. Fig. 1 is a schematic of the formation

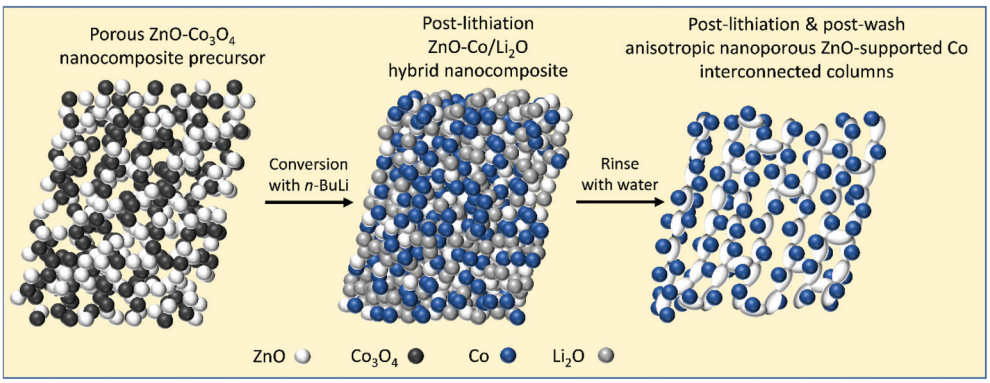

Fig. 1 Schematic illustration of conversion reaction synthesis (CRS) of ZOC with an anisotropic particle structure from the co-precipitated ZnO–Co_3O_4 precursor.

of ZOC with an anisotropic porous structure through the CRS process.

Identification of reaction pathways

In order to understand the actual pathways followed in the course of reactions (3) and (4), synchrotron powder X-ray diffraction (XRD) studies were utilized for phase identification (Fig. 2) and Rietveld refinement for microstructure analysis (Fig. 3) of (a) the pre-lithiation reaction precursors, (b) the post-lithiation intermediate nanocomposite hybrid recovered after reduction, and (c) the nanoporous hybrid recovered after removal of Li_2O (post-lithiation and post-wash). While laboratory XRD data were suitable for preliminary analyses (Fig. S1†), the synchrotron diffraction data were essential to effectively resolve the broad, low-intensity signals from the nanoscale phases produced through these reactions with a sensitivity suitable for quantitative analysis. The synchrotron data were particularly critical for distinguishing between size and strain broadening effects and for probing the anisotropic size broadening exhibited by key phases, as will be discussed in more detail later.

The first step in the analysis is phase identification. It can be readily seen that the precursor mixture prepared through co-precipitation (Fig. 2A) contains only the two phases of wurtzite ZnO and spinel Co_3O_4. The final product (Fig. 2C) is also a two-phase mixture where the two phases are wurtzite ZnO and face-centered cubic Co metal, confirming the formation of a metal–metal oxide hybrid. The intermediate nanocomposite hybrid phase primarily contains ZnO and Co metal, though additional sample-dependent phases of Co_3O_4 (re-oxidized Co metal) and LiOH (reaction product of Li_2O and water) can also be found due to air exposure during sample preparation. The observed diffraction patterns are consistent with all steps of the proposed reaction scheme. The initial reduction step results in the conversion of Co_3O_4 to Co metal. While Li_2O is expected to be a reaction intermediate, diffraction patterns indicate the presence of either Li_2O or LiOH, likely depending on the degree of exposure to moisture during the preparation of the sample for XRD studies. The final step of dissolution in water results in the removal of Li_2O.

The diffraction patterns for these samples can also be used to follow the evolution in sample microstructure throughout these reactions when analyzed through Rietveld refinements that quantitatively model the peak broadening that occurs due to the sample size and strain.[28] The final Rietveld fits are shown on a logarithmic scale in Fig. 3, while the extracted microstructure parameters from these fits are provided in Table 1. Initial trial refinements utilizing isotropic models for size and strain broadening had substantial difficulties in correctly modeling the ZnO peak intensities at all three stages of the reaction (precursor, nanocomposite hybrid intermediate, nanoporous hybrid product) with an error that was *hkl*-dependent rather than 2θ-dependent, as illustrated in Fig. S2–S4.† To address these model limitations, refinements using both anisotropic strain[29] and anisotropic size broadening[30–32] were compared and it was found that diffraction peaks were most effectively fit by utilizing a model for anisotropic size broadening in which the anisotropic shape of ZnO particles was approximated as *c*-axis oriented cylinders that are shorter in the *c*-axis direction than in the in-plane directions together (as illustrated in the insets to Fig. 3) with a conventional isotropic model for strain broadening. As an example, the fit quality with this type of anisotropic shape model (R_{wp} = 6.24) indicated a significant improvement relative to the initial isotropic models (R_{wp} = 7.26) for the final NPo ZOC product.

A second challenge was fitting the asymmetry of the Co metal peaks of the NPo reaction product (Fig. S5†). This was accomplished by modeling the sample as containing two chemically distinct fcc metal phases with different lattice parameters present in an approximate ratio of 2 : 1. The first phase was fit with a crystallite size of 30.3 nm and a conventional lattice parameter (a = 3.546 Å) for pure Co metal. The second was fit with a smaller crystallite size of 5.9 nm and an expanded lattice parameter (a = 3.562 Å), as would be expected for the partial substitution of Zn, resulting in a phase of composition $Co_{1-x}Zn_x$. The value of x could not be effectively determined through the refinement of site occupancies due to the very similar X-ray scattering powers of Co and Zn, though the value of x can be estimated to be approximately 0.03 from the lattice parameter of this phase based on previous diffraction

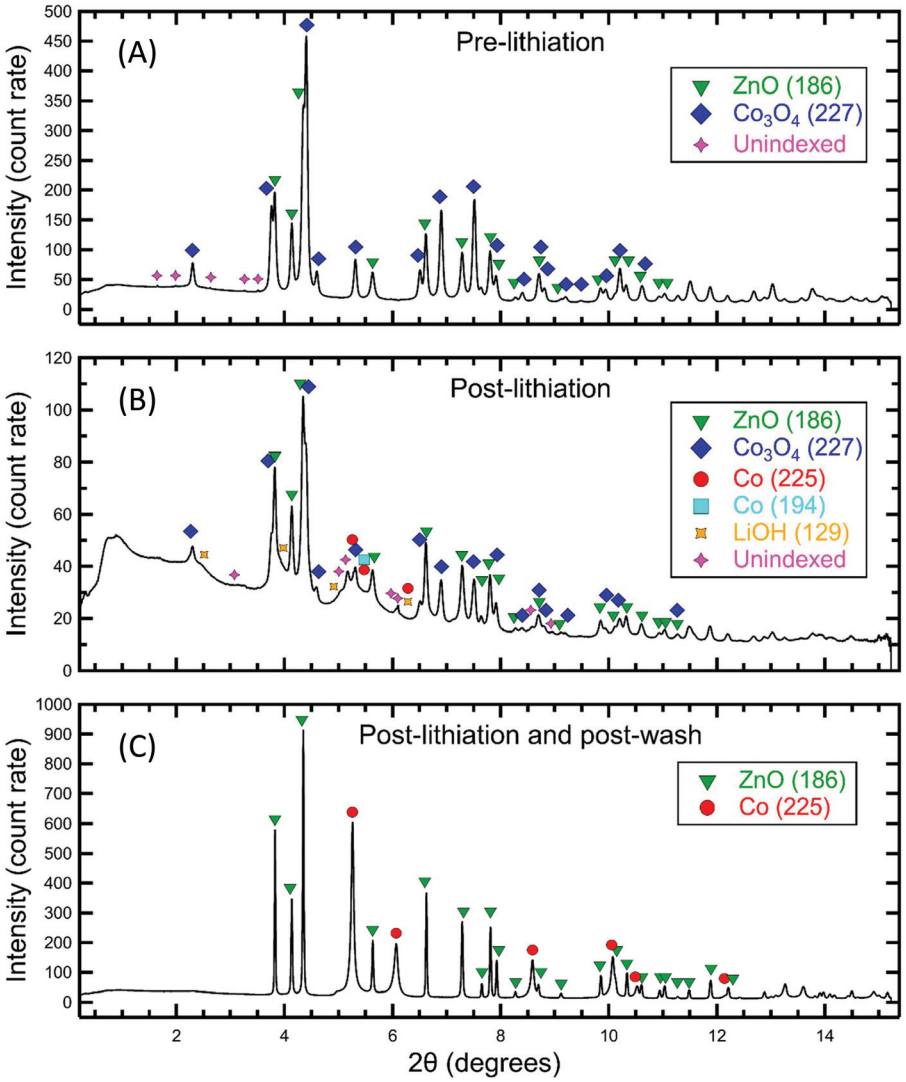

Fig. 2 Phase identification results obtained from synchrotron XRD patterns for (A) the pre-lithiation precursor mixture of ZnO and Co_3O_4, (B) the post-lithiation intermediate nanocomposite with a Li-containing phase, and (C) the post-lithiation and post-wash final NPo ZOC product.

studies of Zn-substituted Co in which it was shown 3% Zn substitution caused an increase in the Co metal lattice parameter by 0.016 Å.[33] This behavior indicates that the partial reduction of Zn occurred during the CRS synthesis and suggests that running the CRS reaction under more or less strongly reducing conditions may enhance or suppress the amount of Zn substitution, respectively, resulting in changes that will likely affect catalytic activity.

Phase quantification done through Rietveld refinement (Table 1) was used to assess mass conservation through the reaction. Though equimolar amounts of Co and Zn are used in the co-precipitation step, the ZnO–Co_3O_4 nanocomposite precursor was found to be 40% Zn and 60% Co (1.5 : 1 Co to Zn mol ratio). Phase fractions in the final product demonstrate that the Co to Zn molar ratio persists through lithiation and rinsing. The loss of some Zn from co-precipitation is attributed to evaporation of Zn during the calcination of the mixed-metal oxalate dihydrate at 420 °C due to the reduction of ZnO to Zn in the presence of organic species and low melting point of Zn (419 °C). TEM-EDX mapping (Fig. S6†) is consistent with the XRD quantification, showing approximately a 1.5 : 1 Co to Zn mol ratio.

Hierarchical structure of NPo composites

Complementary insights into the morphology of primary and secondary particle morphologies can be obtained through electron microscopy studies, including SEM (Fig. 4) and TEM (Fig. 5 and Fig. S6, S7†) studies. Fig. 4A shows that the reaction precursor particles have a prismatic morphology with a size of 1 micron or more and a clear anisotropic particle shape. A close inspection of the precursor particles indicates that they are not dense crystallites but are instead a porous composite. This composite morphology is a consequence of the synthesis method. Although the synthesis was described as a co-precipitation, the precipitation occurred throughout a 24 hours reflux

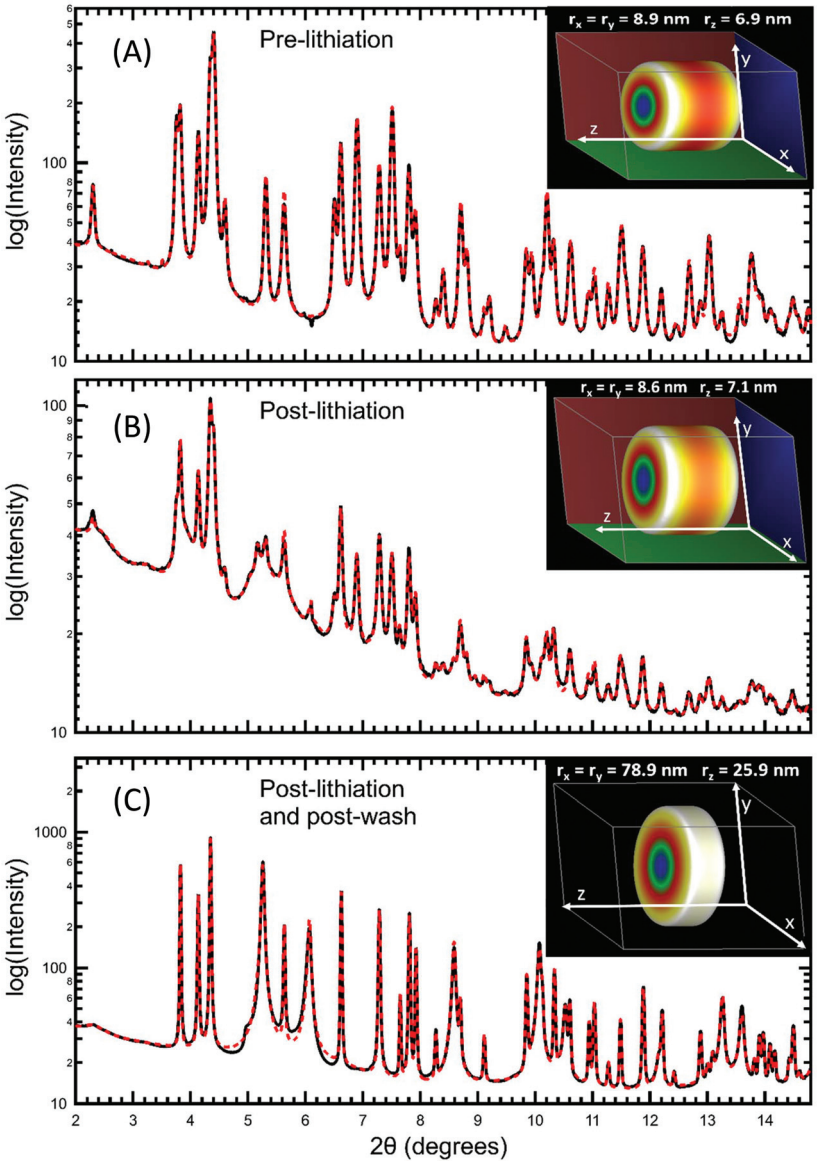

Fig. 3 Data fits to synchrotron XRD patterns obtained through Rietveld refinement incorporating anisotropic size broadening of diffraction peaks based on cylindrical particle shapes for (A) the pre-lithiation precursor mixture of ZnO and Co_3O_4 (R_{wp} = 3.363), (B) the post-lithiation intermediate nanocomposite with a Li-containing phase (R_{wp} = 1.790), and (C) the post-lithiation and post-wash final NPo ZOC product (R_{wp} = 6.240). Insets show the particle shape used for the modeling of anisotropic size broadening.

period, suggesting that particles formed *via* the slow nucleation and growth of crystallites from solution rather than the rapid precipitation of an amorphous matrix. Laboratory XRD data (Fig. S8†) was collected on the precipitate, and it was found to be a single phase Co/Zn metal oxalate dihydrate, $Co_{1-x}Zn_x(C_2O_4)(H_2O)_2$ where x is estimated to be 0.5, indicating Co and Zn are intimately mixed on the atomic scale. After carrying out a calcination step to dehydrate this phase at 420 °C, phase separation is inferred to occur within the precursor particles to produce the nanoscale primary particles of ZnO (~8 nm) and Co_3O_4 (~17 nm) whose size was estimated from our XRD studies. These sizes are consistent with the porosity length scale seen in the SEM data of Fig. 4A.

When the precursor phase is converted to a hybrid nanocomposite of ZnO, Co metal, and Li_2O through reduction with *n*-BuLi, the porosity in the micron-scale particles is greatly reduced, as can be seen in Fig. 4B. This suggests that the Li_2O formed from the oxidation of Li in this reaction resides in close proximity to the Co metal that is the reduction product of Co_3O_4, and that the low density and high prevalence of Li_2O allow it to effectively fill the porosity of the precursor phase. This conclusion is supported by SEM imaging of the final nanoporous hybrid product of ZnO-supported Co (Fig. 4C) from which the Li_2O phase has been removed by washing. It can be clearly seen that the porosity of the particles has been regained. Furthermore, the SEM images of this ZOC product

Table 1 Lattice parameters (Å), phase fractions (weight %), and crystallite radii and lengths (nm) calculated from Rietveld refinements for synchrotron XRD patterns

Sample	Phases (space group)	Lattice parameters (Å)	Phase fractions (wt%)	Crystallite radii/length (nm)
Pre-lithiation precursor mixture of ZnO and Co_3O_4	ZnO (186)	$a = b = 3.25448(2)$ $c = 5.20658(6)$	40.54(5)	$r_x = r_y = 8.88(3)$ $r_z = 6.96(3)$
	Co_3O_4 (227)	$a = b = c = 8.10851(3)$	59.46(5)	16.6(1)
Post-lithiation hybrid nanocomposite	ZnO (186)	$a = b = 3.25422(3)$ $c = 5.20649(8)$	11.4(1)	$r_x = r_y = 8.61(4)$ $r_z = 7.10(3)$
	Co_3O_4 (227)	$a = b = c = 8.11367(9)$	8.9(1)	14.8(1)
	Co (225)	$a = b = c = 3.548(2)$	1.2(1)	3.9(1)
	Co (194)	$a = b = 2.560(2)$ $c = 4.160(8)$	9.4(4)	1.54(2)
	LiOH (129)	$a = b = 3.505(1)$ $c = 4.395(2)$	69.0(4)	2.36(2)
Post-lithiation and post-wash nanoporous ZnO–Co (NPo ZOC)	ZnO (186)	$a = b = 3.24989(1)$ $c = 5.20714(4)$	47(9)	$r_x = r_y = 78.9(1)$ $r_z = 25.9(4)$
	Co (225)	$a = b = c = 3.54635(4)$	35(6)	30.3(7)
	$Co_{1-x}Zn_x$ (225)	$a = b = c = 3.5615(6)$	17(15)	5.9(1)

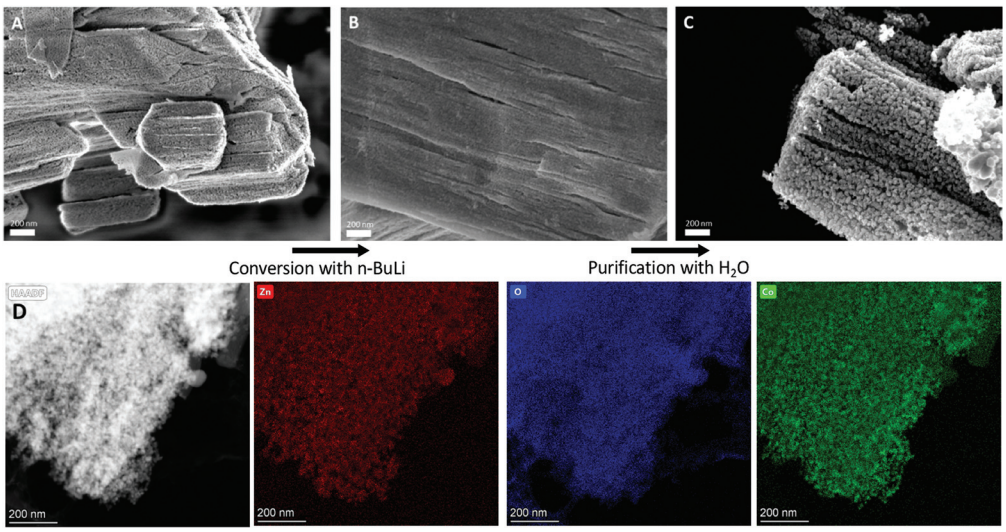

Fig. 4 SEM images of (A) pre-lithiation Co_3O_4–ZnO precursor; (B) post-lithiation Co-ZnO-Li_2O nanocomposite; (C) post-lithiation and post-wash nanoporous ZnO-supported Co. (D) TEM image of post-lithiation and post-wash nanoporous ZnO-supported Co as well as the corresponding EDX maps of (from left to right) Zn, O, and Co showing the uniform distribution of the elements within secondary particles. All images have 200 nm scalebars.

indicate that the primary particle sizes increased relative to the precursor and intermediate stages of the reaction. This is fully consistent with the substantial changes in particle size of both ZnO and Co metal inferred from the XRD analysis (Table 1). Changes in particle size are tentatively attributed to the local heating and concomitant mobility increase that occurs when the surface of Co metal is locally oxidized upon exposure to water during the dissolution process to remove Li_2O. TEM EDX maps of NPo ZOC (Fig. 4D) show a uniform distribution of the elements indicating an intimate mixing of nanoscale ZnO and Co primary particles within the micron-scale secondary particles, though its resolution is insufficient to allow us to directly distinguish between the two metal particles. SEM and TEM images (Fig. 4C and D) clearly illustrate the mesoporous nature of the particles.

More detailed insights into the morphology of the final ZOC product can be obtained from TEM studies (Fig. 5). At low magnification (Fig. S7†), the columnar, anisotropic shape of the particle is again observed. At high magnification (Fig. 5B–D), it can be clearly seen that the primary particle sizes are on the order of 20 nm, as was suggested by size-strain analysis of XRD data. The close proximity of the ZnO and Co

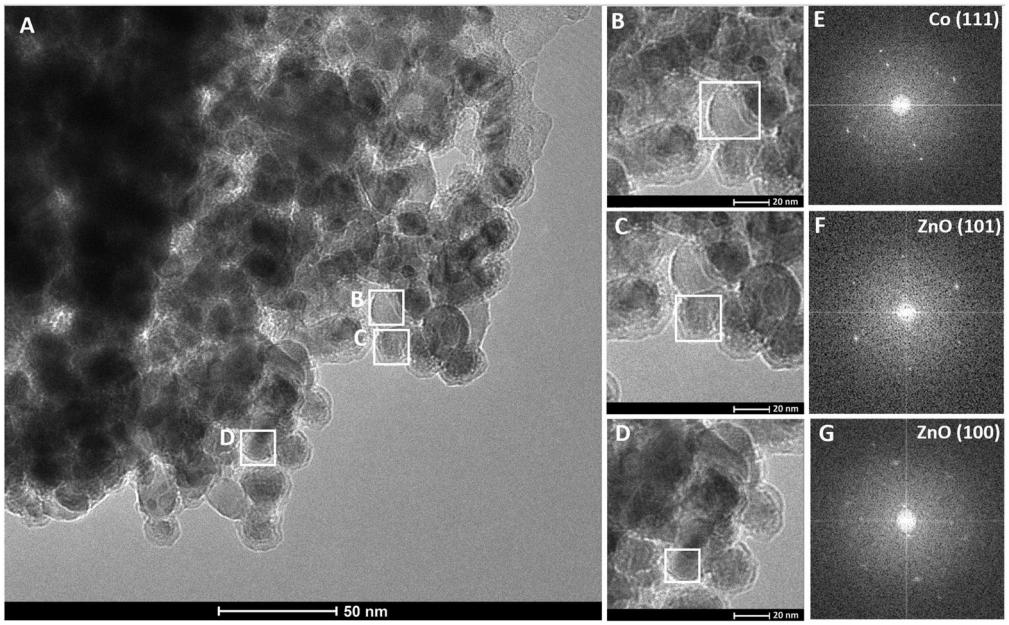

Fig. 5 TEM images of post-lithiation and post-wash nanoporous ZnO-supported Co (A). NPo ZOC has primary particles on the order of 20 nm, as was suggested by size-strain analysis of XRD data. The zoomed in regions of fcc Co and wurtzite ZnO (B–D) show selected area electron diffraction patterns (E–G) that confirm the structure of the ZnO and Co phases, as well as their close proximity demonstrating that they are very well intermixed.

metal phases is confirmed by the selected area electron diffraction (SAED) analysis as shown in Fig. 5E–G where the diffraction patterns are consistent with those of Co and ZnO determined through XRD. The porous structure of the ZOC product is evaluated through BET measurements (Fig. S9†), which indicate a specific surface area of 27.98 $m^2\ g^{-1}$ and a peak pore size of 30 nm. Additionally, the pore size distribution plot shows the regular presence of pore sizes up to ten times larger than the peak value, showing that there are higher-accessibility pathways involving larger diameter pores that facilitate the access of reactive species to the smallest pore diameters.

Temperature stability of NPo composites

One key motivation for the preparation of ZnO–Co metal nanoporous hybrid materials (NPo ZOC) is the expectation for enhanced thermal stability of Co metal in these composite materials relative to that of pure nanoporous Co (NPo Co). We have previously observed that many nanoporous metals prepared by CRS methods, including NPo Co, can rapidly coarsen when heated, resulting in the porosity decreasing until the nanostructure is destroyed. It was found that the coarsening of NPo Co can be detected at temperatures as low as 150 °C [13] though it is difficult to assign a specific temperature threshold for stability due to the lack of a well-defined metric for this property as well as potential preparation-dependent behavior of NPo Co samples.

In order to investigate stability enhancements of NPo ZOC relative to nanoporous Co metal, different fractions of a single NPo ZOC sample were annealed for 3 hours at temperatures ranging from 400–600 °C followed by the collection of XRD data (Fig. 6) to permit the quantification of coarsening through the determination of crystallite size (Table S1†). NPo ZOC shows increased resistance to coarsening when compared with nanoporous Co metal in terms of calculated crystallite sizes (Fig. 7) and peak sharpening (Fig. S11†). Nanoporous Co metal undergoes significant crystallite growth from annealing at 400 °C (1.5 to 35 nm), whereas the Co in NPo ZOC only grows from 7 to 15 nm under the same conditions. The larger initial size of Co in the as-prepared NPo ZOC (7 nm) than in pure NPo Co (1.5 nm) is attributed to transient heating from the more exothermic processes involved in the water-based removal of Li_2O from the former than the alcohol-based removal of LiCl from the later. Additionally, Co coarsening in NPo ZOC appears to taper off at 500 °C (~20 nm), as annealing at 500 and 600 °C produce indistinguishable crystallite sizes, indicating there is a barrier to further coarsening after the initial rearrangements.

BET surface area measurements were also performed on NPo ZOC as-synthesized and after annealing at 400 and 600 °C to demonstrate the stability of the overall structure and retention of porosity (Fig. S10†). While there is an initial decrease in surface area from 27.98 $m^2\ g^{-1}$ to 20.84 $m^2\ g^{-1}$ (as-synthesized *vs.* annealed at 400 °C) that can be attributed to Co coarsening, annealing at 600 °C yields a surface area of 22.61 $m^2\ g^{-1}$. This indicates that the structure is largely unchanged from annealing at 600 °C compared to 400 °C, agreeing with the coarsening behavior evinced from XRD analysis.

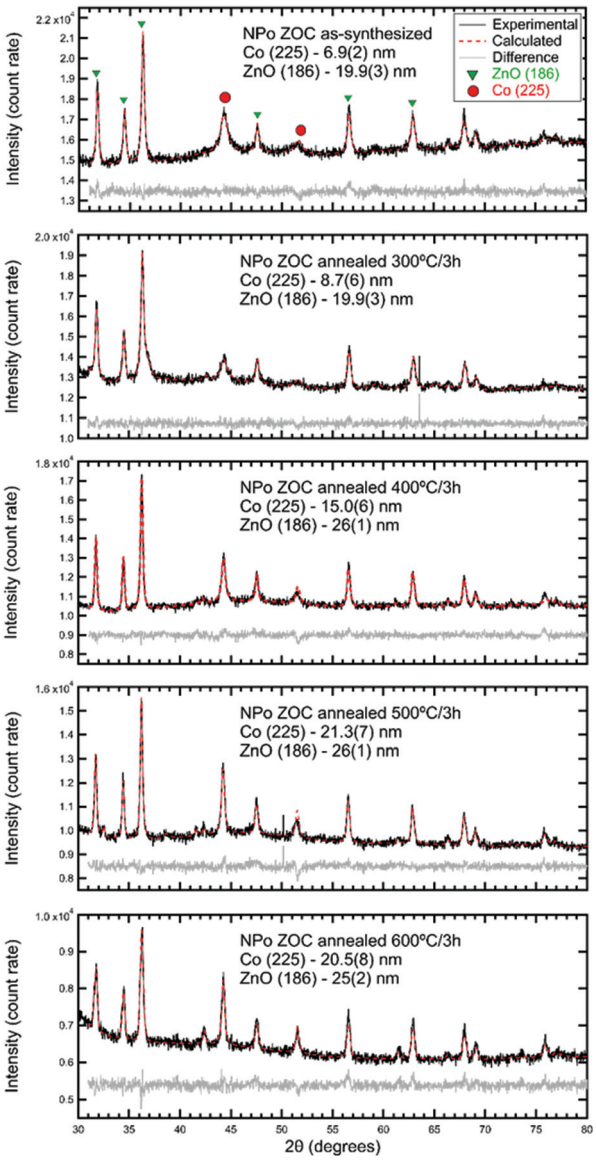

Fig. 6 Data fits from Rietveld refinement on XRD patterns of as-synthesized nanoporous ZnO–Co and after annealing for 3 hours at 300–600 °C. Further phase information and crystallographic parameters provided in Table S1.†

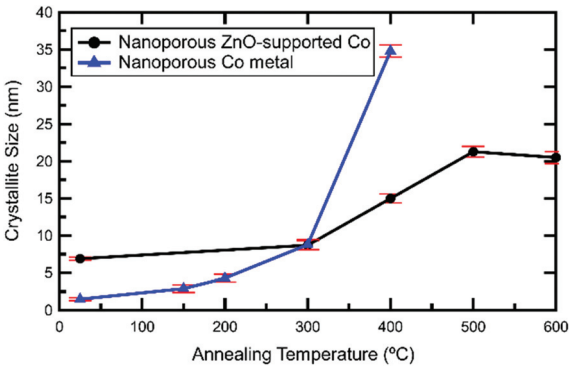

Fig. 7 Comparison of temperature dependent coarsening for nanoporous ZnO-supported Co and nanoporous Co metal. Further data on the effect of temperature on surface area can be found in Fig. S9.†

Catalytic activity testing

The steam reformation of ethanol (SRE) is an important industrial reaction for which improved catalysts are desired, with the overall reaction given below:

$$3H_2O + C_2H_5OH \xrightarrow[\Delta]{\text{catalyst}} 5H_2 + 2CO_2$$
$$\Delta H_{298} = +178\ \text{kJ mol}^{-1} \quad (5)$$

This reaction is typically carried out at a temperature between 200 and 800 °C, depending on the catalyst.[22] It has previously been demonstrated that Co nanoparticles are active catalysts for this reaction when supported on ZnO, and previous catalytic testing at temperatures of 400–500 °C has been described in the literature.[34,35] It is therefore of interest to investigate whether the use of novel NPo ZOC catalysts prepared through CRS methods provide any advantages over traditional NP ZOC catalysts.

Continuous flow catalytic testing of NPo ZOC was carried out at 400 °C based on the enhanced resistance to coarsening observed for this material (relative to nanoporous Co) in the thermal stability testing of the previous section. The distribution of the gaseous products from the SRE reaction on the NPo catalyst as a function of time during continuous flow testing are shown in Fig. 8 with values provided in Table S2.† After the first hour of testing, the only gaseous reaction products present are H_2 and CO_2, present in about a 2 : 1 ratio. With further testing, additional products of CH_4 and CO are observed at fractions of approximately 8 and 2%, respectively. The appearance of CH_4 and CO is accompanied by a decrease in the CO_2 fraction but not the H_2 fraction. Taken together with the latency in the appearance of CH_4 and CO, it appears that these alternate reaction products result from the reduction of CO_2 rather than representing alternate direct products of ethanol decomposition, such as the known transform-

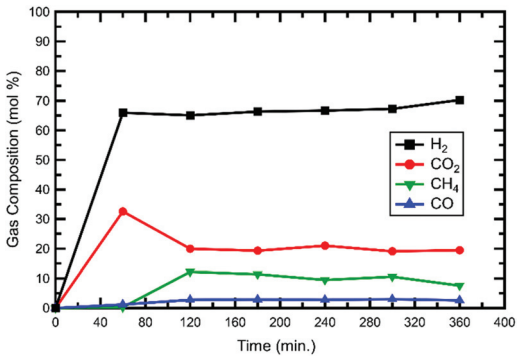

Fig. 8 Composition of product gasses when nanoporous ZOC is used as a heterogeneous catalyst for the steam reformation of ethanol over the course of 6 hours. Tabulated values in Table S2.†

ations of ethanol into ethylene or acetaldehyde.[15,24] The high selectivity of hydrogen production from ethanol using the present catalyst is already comparable to that previously reported for Co NP catalysts, and it is expected that the NPo ZOC selectivity can be further improved through the optimization of reaction conditions (temperature, flow rate, H_2O content).[15,16,23,24]

In addition to testing the selectivity of the NPo ZOC catalyst, the activity of this catalyst was also tested and directly compared to that of a standard formulation for a NP Co metal catalyst that is supported on ZnO[34] measured in the same reactor. Along with having a similar Co : Zn molar ratio, the standard NP Co catalyst used for comparative testing had a similar surface area (26 *vs.* 28 $m^2\ g^{-1}$ for NPo ZOC) to the novel NPo ZOC catalyst. As is shown in Fig. 9, the amount of H_2 produced using the NPo ZOC catalyst exceeds that of the NP Co catalyst at all tested flow rates (40–210 mL min^{-1}), by at least a factor of 3 (Table S3†).

The improvement in catalytic performance is large and suggests that the anticipated advantages of the NPo ZOC catalysts are significant. It is not possible to determine from the present data whether the enhanced performance is due to intrinsic factors (*e.g.*, lowered activation energy, more favorable Co morphology, better cooperativity between catalyst and support) or extrinsic factors (*e.g.*, better accessibility to gas, higher fraction of Co on exposed surface). A major difference between the two catalysts is the anisotropic structure of the NPo ZOC catalyst versus the isotropic structure of the standard catalyst, as the standard catalyst was designed to have the same Co : Zn ratio (1 : 1) and similar specific surface area (approximately 26 $m^2\ g^{-1}$ for the standard catalyst compared to 28 $m^2\ g^{-1}$ for the ZOC catalyst). There are previous cases of anisotropic nanomaterials exhibiting superior catalytic activity when compared to their isotropic forms. For example, dendrimer shaped gold nanoparticles are more efficient catalysts than spherical gold nanoparticles for reducing sudan-1 in the presence of $NaBH_4$.[36] In these situations, the anisotropic form of a catalytic material typically has a higher concentration of more catalytically active crystal facets, increasing catalytic activity.[37] Further investigation is required to discern the exact reason for the NPo ZOC catalyst's higher performance over the standard ZnO-supported Co catalyst, including the role of Zn doped Co present in our materials, but current evidence suggests that the enhanced performance is significantly influenced by the anisotropic ZOC microstructure and the better overall mass transport that it enables.

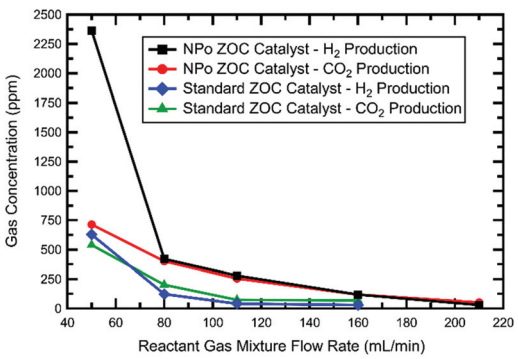

Fig. 9 Concentration profiles of H_2 and CO_2 gas produced by steam reformation of ethanol over a ZnO–Co catalyst at various reactant gas mixture flow rates. Tabulated values are summarized in Table S3.†

Conclusion

It is for the first time demonstrated that conversion reaction synthesis (CRS) can be used to produce hybrid nanoporous structures between metals and non-metals by utilizing custom precursors with components that can be selectively reacted with strong reducing agents such as *n*-BuLi. In the present work, a co-precipitated Co_3O_4–ZnO nanocomposite precursor was used to synthesize nanoporous ZnO-supported Co (NPo ZOC) as a composite material. Combining Co and ZnO in a composite nanoporous material resulted in increased thermal stability of the catalytically active Co metal phase relative to isolated nanoparticles, thus providing an integral support for this catalyst within the nanoporous matrix. NPo ZOC proved to be an effective catalyst for the steam reformation of ethanol at 400 °C, exhibiting complete conversion of ethanol and high selectivity for hydrogen production. The methods described here provide a general and scalable route for designing supported nanoporous catalysts with enhanced performance.

Experimental section

Preparation of Co_3O_4–ZnO nanocomposite precursor

$Co(OAc)_2{\cdot}4H_2O$ (1.136 g) and $Zn(Oac)_2{\cdot}2H_2O$ (1.0 g) were dissolved in deionized water (100 mL) at an equimolar ratio and then a sodium oxalate solution (100 mL, 0.1 M) was added dropwise to the acetate solution while stirring. One mole of sodium oxalate was used per mole of cobalt acetate and zinc acetate combined. Once all of the sodium oxalate was added, the entire solution was reflux for 24 hours. The solution was then poured through a fritted filter funnel to isolate the pink precipitate, which is then washed with an excess of deionized water and then dried. Lastly, the dried precipitate was calcined in air at 420 °C for 4 hours to yield the Co_3O_4–ZnO nanocomposite precursor. This method was adopted from work by Rong *et al.*[38]

Conversion reaction synthesis of NPo ZOC

In an argon glovebox, the Co_3O_4–ZnO nanocomposite precursor was dispersed in hexane (10 mL per gram precursor) that was dried with size 3A molecular sieves. *N*-BuLi solution in hexane (25 mL per gram precursor, 1.6 M) was then slowly added to the precursor dispersion at 1.25 times the minimum stoichiometric amount needed to complete the reaction. The reaction was run for 24 hours at room temperature without stirring before the mixture is passed through a fritted filter

funnel to collect the resulting Co-ZnO-Li_2O nanocomposite powder. In the filter funnel, the nanocomposite was rinsed with hexane before drying. The nanocomposite was then dropped into 300 mL of argon-sparged deionized water without exposure to air and stirred for 60 seconds to remove the Li_2O. The leftover powder was then filtered, rinsed with excess air-free water and dried to yield NPo ZOC.

Synchrotron X-ray diffraction (XRD) analysis

Synchrotron X-ray diffraction (XRD) data were collected in Debye–Scherrer geometry at the National Synchrotron Light Source-II (NSLS-II), Brookhaven National Lab at a wavelength of λ = 0.1877 Å (66.054 keV) on beamline 28-ID-2, X-ray powder diffraction (XPD), with a 2D area detector (Si PerkinElmer, 2040 × 2048 pixel array, 200 × 200 μm pixel size). The sample-to-detector distance was 1566 mm, providing a Q_{max} = 8.9 $Å^{-1}$ (d_{min} = 0.7 Å). Due to the samples' sensitivity to air and moisture, powders were handled in an argon glovebox and sealed with epoxy in 1.1 mm diameter Kapton® capillaries. 10–30 seconds collection times were used with a 0.1 second frame acquisition time for all scans. Collection times were varied to achieve the best signal-to-noise for samples with different packing densities.

Instrument geometry (*e.g.*, sample-to-detector distance, detector *x*, *y*, *z* rotations) was determined using the calibration tool in pyFAI (python Fast Azimuthal Integration) with a Ni ($Fm\bar{3}m$, a = 3.5329 Å) reference material.[39] 2D images of the Debye–Scherrer rings were integrated to 1D XRD patterns using pyFAI's integration tool. Phase identification was done using search and match software (Jade, version 9) with the International Center for Diffraction Data (ICDD) database, as well as indexing methods in Jade. The TOPAS[40] software package (Version 6, Bruker AXS) was used for Pawley[41] and Rietveld refinements.[40,42] Pawley fitting of Ni was done to determine the instrument peak shape profile to be a modified Thompson–Cox–Hastings pseudo-Voigt (TCHZ) function. A second-order polynomial was used to account for the oblique incidence effect, colloquially termed penetration, since pyFAI does not provide a correction. The coefficients of the polynomial were determined by fitting the XRD data on the Ni reference material and considering the peak center offsets as part of the instrument profile, such that the coefficients are then fixed when fitting the experimental data discussed. Rietveld refinements on experimental data were performed for quantitative phase analysis, providing phase fractions and microstructural details (crystallite size, lattice microstrain). Examples of specific fitting parameters can be found in TOPAS input files provided in the ESI.†

Preparation of standard catalyst sample

A previously studied ZnO-supported Co catalyst formulation acted as a standard sample for comparison to the ZOC sample. The standard sample was prepared according to Llorca, *et al.*[34] by the incipient wetness method from an aqueous solution. Kadox® 911 ZnO and $Co(NO_3)_2$ were combined to achieved a mixture with a 1 : 1 molar ratio of Zn to Co. Deionized water was then added to the powder mixture at ~10 mL g^{-1} of powder and the mixture was hand stirred for at least 10 minutes. After mixing, the solution was dried under vacuum at 100 °C for 4 hours and then calcined at 400 °C under normal atmospheric conditions for an additional 4 hours.

Materials characterization

Laboratory X-ray diffraction (XRD) patterns of all samples were collected using a Bruker D2 Phaser powder diffractometer using Cu Kα radiation (λ = 1.5418 Å, 40 kV, 40 mA) in a 2θ range from 10–80° with a scan rate of 0.01° s^{-1}. In an argon glovebox, powder samples were loaded into circular sample holders and sealed with Kapton® tape to prevent air contamination. Lab XRD patterns were analyzed similarly to synchrotron XRD patterns, though with a fundamental parameters model to describe the instrument (0.6 mm divergence slit, 20 mm sample length, 250 mm beam path length, 2.5° Soller slits) and source (Cu Kα) line profile contributions.[43,44] Examples of fitting parameters can be found in the TOPAS input files provided in the ESI.†

SEM images were acquired with a Zeiss Sigma 500 scanning electron microscope and TEM images were obtained at 200 keV acceleration voltage on a ThermoFisher Talos 200X system and a high-angle annular dark-field detector was used for EDX mapping. BET analysis was conducted with N_2 adsorption–desorption isotherms measured with an ASAP 2020 surface area and porosity analyzer. Each sample was loaded into a measurement cell in a glovebox and then closed with Parafilm to protect it from oxygen as it is transferred to the analyzer. Once inserted into the analyzer, each sample was degassed under vacuum at 60 °C for 12 h. N_2 adsorption–desorption isotherms were collected at 78 K (liquid nitrogen temperature). The isotherm was then analyzed with the native ASAP Sorption Analyzer software to calculate the specific surface area and cumulative pore volume of each sample.

Heterogeneous catalyst testing

Catalytic testing on the NPo ZOC was conducted with an apparatus containing a flow controller system, reactant syringe pump system, vaporizer, and reactor unit. The flow system consisted of two Dwyer Instruments VFA-series flow controllers to accurately control gas flow into the system (Ar, N_2, H_2, *etc.*). The pump system consisted of a DUAL-NE-1000X continuous infusion syringe pump fitted with a 50 mL syringe filled with a water/ethanol solution to provide a constant and precise flow of the reactant mixture into the vaporizer. The ZOC catalyst was arranged in a fixed-bed system by combining 100 mg of powder with quartz wool and packing it into a 3 mm ID quartz tube which was then placed inside of a tube furnace which controlled the operating temperature. Prior to the experiments, the system was purged with argon gas for 1 hour, then the catalyst was activated by *in situ* reduction in flowing 5% H_2–Ar gas (50 mL min^{-1}) at 400 °C for 1 hour. Afterwards, the system was purged with Ar gas again for 1 hour (50 mL min^{-1}). Then, the reactant pump was activated and 3 : 1 molar ratio of H_2O

to ethanol was pumped into the vaporizer at 1 mL h^{-1} to be heated to 130 °C and fed into the reactor by the Ar gas flow. For variable gas flow tests the liquid flow rate was set to 1 μL min^{-1} which ensures a starting reactant gas ratio of 50 Ar to 1 EtOH + H_2O vapor. When increasing the reactant gas mix flow rate, both the Ar flow and the liquid reactant flow to the vaporizer are individually increased to maintain this ratio.

Gas chromatography (GC, SRI 8610C, SRI) with a molecular sieve 5A and a HaySep D column using Ar as the carrier gas was used to quantify the gaseous products of the SRE catalyst test. All gas products were sampled from the reactor manually by diverting the flow of the exhaust gasses into an air-tight syringe and injected into the GC. 20 mL of gas was sampled at a time every hour for 6 hours. After injection, the gasses are transferred to the GC columns and quantified with a thermal conductivity detector (TCD) for H_2 detection and a flame ionization detector (FID) equipped with a methanizer for CO, CO_2 and C1–C6 hydrocarbon detection. The GC is calibrated with calibration gas mixtures (Precision Calibration Mixtures, Praxair). The standards consist of CO (101 ppm), methane (101 ppm), ethylene (200 ppm), ethane (100 ppm), H_2 (98.8 ppm), CO_2 (400 ppm), O_2 (2500 ppm) and N_2 (1700 ppm).

Author contributions

C.M.C. and V. P. prepared samples, collected laboratory XRD patterns and SEM/TEM images, and performed BET surface area measurements. A.A.C. collected synchrotron diffraction data and analyzed all diffraction data. T.K. and D.P.F. performed catalytic reaction measurements. P.L. and P.G.K. supervised the study. C.M.C., A.A.C, P.G.K, and P.L. prepared the manuscript with contributions from all authors.

Conflicts of interest

There are no conflicts to declare.

Acknowledgements

This work was supported as part of GENESIS: A Next Generation Synthesis Center, an Energy Frontier Research Center funded by the U.S. Department of Energy, Office of Science, Basic Energy Sciences, under award number DE-SC0019212. This research used beamline 28-ID-2 (XPD) of the National Synchrotron Light Source II, a U.S. Department of Energy (DOE) Office of Science User Facility operated for the DOE Office of Science by Brookhaven National Laboratory under contract no. DE-SC0012704. This work was performed in part at the San Diego Nanotechnology Infrastructure (SDNI) of UCSD, a member of the National Nanotechnology Coordinated Infra-structure (NNCI), which is supported by the National Science Foundation (grant ECCS-1542148).

References

1 S. Fatima, S. I. Ali, D. Younas, A. Islam, D. Akinwande and S. Rizwan, *MRS Commun.*, 2019, **9**, 27–36.
2 C. Gregor, M. Hermanek, D. Jancik, J. Pechousek, J. Filip, J. Hrbac and R. Zboril, *Eur. J. Inorg. Chem.*, 2010, **2010**, 2343–2351.
3 S. Özkar, *Appl. Surf. Sci.*, 2009, **256**, 1272–1277.
4 S. Navalón and H. García, *Nanomaterials*, 2016, **6**, 123.
5 R. M. Rioux, H. Song, J. D. Hoefelmeyer, P. Yang and G. A. Somorjai, *J. Phys. Chem. B*, 2005, **109**, 2192–2202.
6 Q.-L. Zhu and Q. Xu, *Chem*, 2016, **1**, 220–245.
7 C. Spöri, J. T. H. Kwan, A. Bonakdarpour, D. P. Wilkinson and P. Strasser, *Angew. Chem., Int. Ed.*, 2017, **56**, 5994–6021.
8 W. Luc and F. Jiao, *ACS Catal.*, 2017, **7**, 5856–5861.
9 C. Zhu, Z. Qi, V. A. Beck, M. Luneau, J. Lattimer, W. Chen, M. A. Worsley, J. Ye, E. B. Duoss, C. M. Spadaccini, C. M. Friend and J. Biener, *Sci. Adv.*, 2018, **4**, eaas9459.
10 Y. Ding and M. Chen, *MRS Bull.*, 2009, **34**, 569–576.
11 M. Raney, *US Pat.*, 1628190A, 1927.
12 Y. C. K. Chen-Wiegart, S. Wang, Y. S. Chu, W. Liu, I. McNulty, P. W. Voorhees and D. C. Dunand, *Acta Mater.*, 2012, **60**, 4972–4981.
13 C. M. Coaty, A. A. Corrao, V. Petrova, P. G. Khalifah and P. Liu, *J. Phys. Chem. C*, 2019, **123**, 17873–17883.
14 X. Zhang and Y. Ding, *Catal. Sci. Technol.*, 2013, **3**, 2862–2868.
15 J. Llorca, P. R. de la Piscina, J. Sales and N. Homs, *Chem. Commun.*, 2001, **7**, 641–642.
16 P. Munnik, P. E. De Jongh and K. P. De Jong, *Chem. Rev.*, 2015, **115**, 6687–6718.
17 M. M. Schubert, V. Plzak, J. Garche and R. J. Behm, *Catal. Lett.*, 2001, **76**, 143–150.
18 J. Erlebacher, M. J. Aziz, A. Karma, N. Dimitrov and K. Sieradzki, *Nature*, 2001, **410**, 450–453.
19 I. McCue, E. Benn, B. Gaskey and J. Erlebacher, *Annu. Rev. Mater. Res.*, 2016, **46**, 263–286.
20 Z. Zhang, Y. Wang, Z. Qi, W. Zhang, J. Qin and J. Frenzel, *J. Phys. Chem. C*, 2009, **113**, 12629–12636.
21 C. Coaty, H. Zhou, H. Liu and P. Liu, *ACS Nano*, 2018, **12**, 432–440.
22 M. S. Batista, R. K. S. Santos, E. M. Assaf, J. M. Assaf and E. A. Ticianelli, *J. Power Sources*, 2004, **134**, 27–32.
23 J. Y. Z. Chiou, W. Y. Wang, S. Y. Yang, C. L. Lai, H. H. Huang and C. B. Wang, *Catal. Lett.*, 2013, **143**, 501–507.
24 J. Llorca, N. Homs, J. Sales and P. Ramírez de la Piscina, *J. Catal.*, 2002, **209**, 306–317.
25 P. K. Samanta and S. Mishra, *Mater. Lett.*, 2013, **91**, 338–340.
26 J. I. Sohn, W. K. Hong, S. Lee, S. Lee, J. Ku, Y. J. Park, J. Hong, S. Hwang, K. H. Park, J. H. Warner, S. Cha and J. M. Kim, *Sci. Rep.*, 2014, **4**, 5680.
27 Z. L. Wang, *J. Phys.: Condens. Matter*, 2004, **16**, R829.
28 D. Balzar and H. Ledbetter, *J. Appl. Crystallogr.*, 1993, **26**, 97–103.

29 P. W. Stephens, *J. Appl. Crystallogr.*, 1999, **32**, 281–289.
30 D. Ectors, F. Goetz-Neunhoeffer and J. Neubauer, *J. Appl. Crystallogr.*, 2015, **48**, 189–194.
31 D. Ectors, F. Goetz-Neunhoeffer and J. Neubauer, *J. Appl. Crystallogr.*, 2015, **48**, 1998–2001.
32 D. Ectors, F. Goetz-Neunhoeffer and J. Neubauer, *Powder Diffr.*, 2017, **32**, S27–S34.
33 T. Takayama, S. Shinohara, K. Ishida and T. Nishizawa, *J. Phase Equilib.*, 1995, **16**, 390–395.
34 J. Llorca, P. Ramírez De La Piscina, J. A. Dalmon, J. Sales and N. Homs, *Appl. Catal., B*, 2003, **43**, 355–369.
35 E. Martono, M. P. Hyman and J. M. Vohs, *Phys. Chem. Chem. Phys.*, 2011, **13**, 9880–9886.
36 G. P. Sahoo, D. K. Bhui, D. Das and A. Misra, *J. Mol. Liq.*, 2014, **198**, 215–222.
37 J. A. Dumesic, G. W. Huber and M. Boudart, in *Handbook of Heterogeneous Catalysis*, Wiley-VCH Verlag GmbH & Co. KGaA, Weinheim, Germany, 2008, DOI: 10.1002/9783527610044.hetcat0001.
38 F. Rong, J. Zhao, P. Su, Y. Yao, M. Li, Q. Yang and C. Li, *J. Mater. Chem. A*, 2015, **3**, 4010–4017.
39 G. Ashiotis, A. Deschildre, Z. Nawaz, J. P. Wright, D. Karkoulis, F. E. Picca and J. Kieffer, *J. Appl. Crystallogr.*, 2015, **48**, 510–519.
40 A. A. Coelho, *J. Appl. Crystallogr.*, 2018, **51**, 210–218.
41 G. Pawley, *J. Appl. Crystallogr.*, 1981, **14**, 357–361.
42 H. M. Rietveld, *J. Appl. Crystallogr.*, 1969, **2**, 65–71.
43 R. W. Cheary and A. Coelho, *J. Appl. Crystallogr.*, 1992, **25**, 109–121.
44 R. W. Cheary, A. A. Coelho and J. P. Cline, *J. Res. Natl. Inst. Stand. Technol.*, 2004, **109**, 1–25.